ARTICLE

Cluster Beam Deposition of Lead Sulfide Nanocrystals into Organic Matrices

Adam M. Zachary, Igor L. Bolotin, Daniel J. Asunskis, Amanda T. Wroble, and Luke Hanley*

Department of Chemistry, University of Illinois at Chicago (m/c 111), Chicago, Illinois 60607-7061

ABSTRACT Lead sulfide nanocrystals (PbS NCs) were codeposited into two organic films, titanyl phthalocyanine (TiOPc) and α-sexithiophene, using cluster beam deposition (CBD). NCs of average diameters of ~3−4 nm were evenly distributed in these organic films with average particle spacings of ~4 nm, as determined by transmission electron microscopy. The film composition and NC surface chemistry were monitored by X-ray photoelectron spectroscopy (XPS) and other methods. Pb:S stoichiometry in the NC/TiOPc film was determined by XPS to correspond to the PbS cubic rock salt structure. Soft-XPS using 200 eV energy photons determined the NC−organic surface chemistry by resolving the S 2p core level into four distinct components for sulfur. The soft-XPS results found that the PbS NC surface chemistry could be tuned by varying the H_2S/Ar gas ratio within the CBD source.

KEYWORDS: lead sulfide • nanocrystal • cluster beam deposition • titanyl phthalocyanine • X-ray photoelectron spectroscopy

I. INTRODUCTION

Lead sulfide nanocrystal (PbS NC)-containing films are under consideration for use as the near-IR-active layer in multijunction photovoltaics (1). These lead chalcogenide NCs have size-tunable band gaps across the near-IR (2) and large extinction coefficients (3). The high electron affinity of PbS NCs is expected to further enhance charge transfer within their photovoltaic films (4). Similar arguments can be made for PbSe NCs, whose optical absorption is more toward the visible (2).

PbS NCs may also allow a new mechanism of photovoltaic activity: the production and capture of multiple excitons for each absorbed solar photon, which would allow the photovoltaic efficiency to approach 50% even without heterojunctions (5, 6). Multiple exciton generation has been claimed for PbS, PbSe, and other semiconductor NCs in solution (7), but other results have called into question the existence of multiple exciton generation in CdSe and CdTe NCs (8). Nevertheless, independent work has confirmed multiple exciton generation for at least PbSe NCs, albeit at lower efficiencies and possibly independent of the quantum confinement afforded by NCs (9).

Regardless of the viability of multiple exciton generation in NCs, high efficiency photovoltaic devices composed of lead chalcogenide NCs have yet to be demonstrated. Devices composed of PbS or PbSe NCs embedded in organic matrices have shown only low efficiencies (10−15). Films of closely packed PbS and PbSe NCs have displayed somewhat higher photovoltaic efficiencies (although absolute efficiencies remained low) (1, 16, 17). Nevertheless, the rapid progress in increasing the overall solar-to-electrical conversion efficiency of PbS and PbSe NC photovoltaics from <0.1% to ~2% shows great promise (1).

* Corresponding author. E-mail: LHanley@uic.edu.
Received for review May 5, 2009 and accepted July 17, 2009

DOI: 10.1021/am900301x

The surface chemistry of PbS and PbSe NCs is known to exert a strong effect on the photovoltaic performance by modulating the surface density of states, charge-transfer efficiency, excited-state lifetimes, and other phenomena (7). Annealing or chemical treatments of PbS NC−organic composites removed capping ligands and led to large enhancements in the photovoltaic efficiency (13−15). Such effects were also observed for closely packed PbS and PbSe NC films, whose photovoltaic efficiencies were increased dramatically by optimization of the surface to minimize the presence of oxygenated species such as sulfates (1, 16, 17). By contrast, PbS NC films with oxides at their surface behave as photodetectors rather than photovoltaics (1). It has been further argued that covalent organic linkages between adjacent ligands were responsible for enhancing the photovoltaic efficiency (16). Surface passivation of PbS NCs also strongly affects their linear and nonlinear (18) optical properties in the visible and near-IR.

PbS NCs are most commonly synthesized with capping agents via colloidal (19) or other liquid-phase methods (18). This paper describes methods for the preparation of PbS NCs via a gaseous deposition strategy known as cluster beam deposition (CBD), which was described in a preliminary report (20). The advantages of gaseous deposition techniques include direct control of the film thickness and indirect control of film morphology, both especially useful for the preparation of ~300-nm-thick films required for PbS NC-containing photovoltaics (1). This paper also demonstrates the ability to control PbS NC surface chemistry by CBD. Additional advantages of CBD include compatibility with other gaseous deposition methods employed in photovoltaic device preparation, oxidation reduction, and reduction of NC agglomeration within the film.

A number of other gaseous deposition techniques have been investigated for the synthesis of PbS and other semiconductor nanostructures. A modified electrospray organometallic chemical vapor deposition technique was used to

Published on Web 07/31/2009

fabricate CdSe NCs in a ZnS matrix (21). PbS and other NCs were fabricated by thermospray nebulization of monodispersed droplets of aqueous/organic semiconductor salt solutions, which form solid NCs upon solvent evaporation (22). PbS NCs were also synthesized from γ-irradiated polymerization of metal−salt nanofibers and subsequent exposure to H_2S (23). Finally, crystalline PbS NCs of various sizes have been synthesized by the condensation of a thermally generated PbS vapor (24, 25).

Most CBD sources employ the method initially described by Haberland et al. (26) in which metal atoms are magnetron sputtered into a rare-gas flow, which serves the dual purpose of cooling and condensing the atoms into clusters as they are swept out of the exit aperture of the source. CBD produces high-density beams of clusters, permits control over the particle flux and coverage, and can be scaled up for commercial processing (26−28).

CBD is used here for the gaseous deposition of PbS NCs codeposited into an evaporated organic, which controls the NC size distribution, surface chemistry, and shape by preventing unwanted agglomeration (20). Two different organic matrices were used in PbS NC/organic film fabrication, α-sexithiophene (6T) and titanyl phthalocyanine (TiOPc), verifying that the CBD method is applicable to any evaporable matrix. 6T was chosen because it absorbs in the visible region and it has a long conjugated backbone ideal for charge generation and charge transfer in photovoltaics and other devices (29). 6T has also been employed as the active layer in Schottky diodes, field effect transistors and photovoltaics. TiOPc displays a strong Q-band absorbance in the visible region of the absorbance spectrum, making phthalocyanines good candidates for electron donors in heterojunction organic photovoltaics (30). TiOPc was studied in this case because it functions as an excellent material for charge-carrier photogeneration in photovoltaic devices and, when combined with embedded PbS NCs, might produce a significant photocurrent.

II. EXPERIMENTAL SECTION

A. CBD. Figure 1 shows the experimental apparatus used for CBD. The CBD source sputters a target via a direct current (dc) magnetron mounted on a linear translator with a 100 cm range that allows the path length from the magnetron to the expansion zone to be varied. The gas inputs and differentially pumped outer chamber of a commercial CBD source (Nanogen-50; Mantis Deposition Ltd., Oxfordshire, U.K.) were modified for these experiments. The input for the sputtering gas, Ar, was adapted to include a reactive gas via an added connection from the mass-flow control valves in Figure 1. The CBD source consists of an ethanol-cooled inner chamber and a differentially pumped outer chamber that nested within the main experimental chamber. The length of the outer chamber was shortened from 23 to 14 cm to move the CBD source closer to the sample. The ethanol-cooled inner chamber houses a water-cooled dc magnetron, which typically operates under a pressure of ∼10−30 mTorr at 28−35 W power, depending on the gas flow rates.

Pb atoms were produced by dc-magnetron sputtering of a Pb target via Ar gas at a flow near 1 sccm regulated by a mass-flow controller (M100B; MKS Instruments, Andover, MA). Metal atoms are thought to nucleate via three-body collisions with

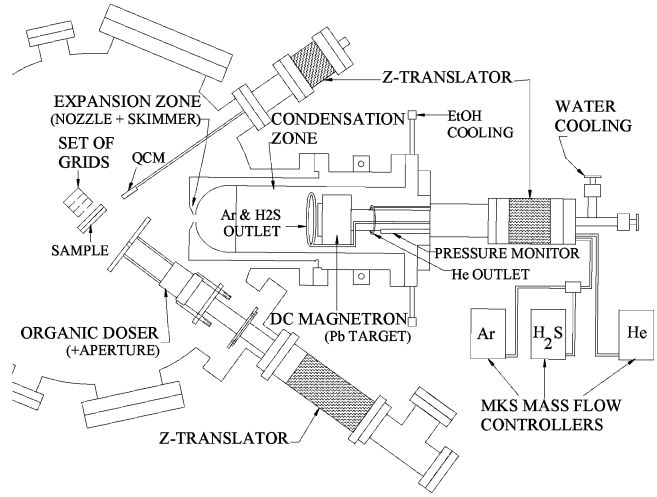

FIGURE 1. Experimental setup with a CBD source connected to mass-flow controllers, an organic doser with an aperture for film size control, a QCM for film thickness monitoring, and a Faraday cup positioned above the sample for current and beam energy determination.

neighboring atoms in CBD to form dimers that serve as the site for condensation to larger clusters (26). The reaction of Pb to form PbS was initiated by the flow of hydrogen sulfide gas (H_2S) at rates of 0.5−2.0 sccm as regulated by another flow controller (1479A; MKS Instruments) into the same outlet above the Pb target as that used for Ar gas input. Overall, H_2S and Pb reacted and condensed to form gaseous $(PbS)_n$ clusters as they passed from the ∼250 K ethanol-cooled inner chamber (labeled the CONDENSATION ZONE) and then exited through the nozzle toward the skimmer (labeled the EXPANSION ZONE). The outer chamber was equipped with a 300 L/s turbomolecular pump attached to the inner chamber. The pressure differential between the inner (10^{-2} Torr) and outer (10^{-5} Torr) chambers also affected $(PbS)_n$ cluster formation during expansion. The skimmer extracted the central portion of the gaseous mixture including the $(PbS)_n$ cluster beam, which entered the main chamber (pumped by another 300 L/s turbomolecular pump) and traveled ∼18 cm from the skimmer to deposit onto the substrate, which could be electrically isolated for current measurements. The base pressure was $\sim 10^{-8}$ Torr for the main chamber in which the substrate was located.

B. Organic Doser. Simultaneous with cluster deposition, either 6T (CAS 88493-55-4, Sigma-Aldrich) or TiOPc (CAS 26201-32-1, Sigma-Aldrich) was evaporated onto the substrate from an organic doser (LTE 11000K, 1 cc; Kurt J. Lesker) to form a PbS NC−organic film. The temperature of the organic doser ranged from 423 to 483 K for the evaporation of 6T and from 563 to 603 K for that of TiOPc. These doser temperatures were controlled to provide a fluence of $\sim 7 \times 10^{15}$ neutrals/cm^2 for either 6T or TiOPc. The sample remained in the center of the deposition chamber and at a constant distance of 10 cm from the organic doser throughout all experiments. The magnetron path length was the only distance varied during experiments.

C. Deposition Times, Substrates, and Sample Transfer. All films for X-ray photoelectron spectroscopy (XPS) studies were deposited for 1 h onto Au-coated Si substrates. The films for transmission electron microscopy (TEM) were deposited on specialized C grids (3620c-MB; SPI Supplies, West Chester, PA) for 30 min. Elemental and chemical analyses were done on a minimum of three replicate samples. The sample was stored in a container under a N_2 atmosphere during transfer from the deposition chamber to the XPS chamber. Films for soft-XPS analysis were analyzed after 1−2 days of storage. Films for TEM analysis were deposited on C grids, which were placed in the storage container and transferred to the TEM load lock within

15 min. Samples prepared for UV/vis absorbance were deposited on indium−tin oxide (ITO)-coated glass (31).

D. Cluster Beam Diagnostics. The energy distribution of the cluster beam was quantified by retarding field measurements using a set of grids to monitor the charged particle current. All such measurements were done with the organic doser off. The Faraday cup used for current measurement consisted of three stainless steel plates (2.5 × 3.7 cm) with a 1.2-cm-diameter hole in their center and another stainless steel plate that served as a charge collector. Ni mesh (bm0117-01-N, 88% transmission; Industrial Netting, Minneapolis, MN) was placed over each hole. The first and third plates were grounded, with the middle plate biased during the retarding of potential measurement experiments.

A quartz crystal microbalance ($QCM_{OFFAXIS}$; model SQC-222, Sigma Instruments, Fort Collins, CO) sits adjacent to the sample in Figure 1 and 35° off axis from the CBD source. It was used to measure the flux of evaporated molecules and the resultant film thickness (32). A second QCM, QCM_{ONAXIS}, was perpendicular to the CBD source and was modified to allow characterization of the CBD source using a retarding field grid, with two Teflon wafers sandwiching and isolating a Ni grid. The $QCM_{OFFAXIS}$ was also used to monitor the deposition process and calibrate film thicknesses (31, 32). The PbS NC−organic film deposition rates onto $QCM_{OFFAXIS}$ were obtained from QCM frequency changes, which were converted to thicknesses via calibration based upon measurements of thicker PbS NC−organic films with a surface profilometer (P1 long scan surface profiler; KLA-Tencor, Milpitas, CA). The film used for calibration of the QCM induced a frequency change of 3792 Hz and was found by the surface profilometer to have a thickness of 209 ± 5 nm.

E. XPS. Photoemission spectra were collected using monochromatic Al K_α radiation, as well as 200 eV soft X-radiation produced at a synchrotron facility. Monochromatic Al K_α XPS were recorded after <10 min of air exposure following deposition, using a separate instrument described previously (33). All core level spectra were calibrated to C 1s at 285.0 eV and were recorded with a pass energy of either 22 or 44 eV. The instrument resolution calibrated by the Ag $3d_{5/2}$ core level spectrum was of 0.83 eV full width half-maximum (fwhm) at a 22 eV pass energy and 1.27 eV fwhm at a 44 eV pass energy. Peak-fitting parameters for the C 1s and O 1s core level spectra from TiOPc have been previously reported (31) and are not discussed in detail here.

Soft-XPS using 200 eV photons was performed at the Mark V Grasshopper beamline of the Aladdin storage ring at the Synchrotron Radiation Center of the University of Wisconsin—Madison. A double-pass cylindrical mirror analyzer set at a pass energy of 20 eV was used to measure the kinetic energy of photoelectrons, giving a 0.72 eV fwhm for the Au $4f_{7/2}$ core level of a Au film. Because of the shallow escape depth of photoelectrons at photon energies in the soft-XPS regime, a signal from the underlying Au substrate was not present, so all core-level spectra were calibrated to the S $2p_{3/2}$ feature because of sulfide in the NC core (S_{core}) at 161.0 eV binding energy (34−37). The soft-XPS data had a nonlinear background subtracted, which was approximated using a fifth-order polynomial equation, and then the data were smoothed using a three-point boxcar filter before peak fitting (36, 38−40). Peak fitting for the soft-XPS data was performed using freeware (XPSPeak 4.1, The Chinese University of Hong Kong, www.phy.cuhk.edu.hk/~surface/XPSPEAK). Elemental fractions were determined from XPS core level peak areas via established methods (41). The films prepared for XPS analysis were ~10 nm thick.

F. TEM. TEM analyses were carried out on microscopes operated at 200 and 300 keV primary electron beam energy (JEOL-2010F and JEOL-3010, respectively; JEOL USA). Film thicknesses for TEM were ~3 nm. NC size distributions were determined using imaging software (Paint.NET, www.getpaint.net). NCs in the TEM image were individually circled, and a horizontal line was drawn to measure their diameters, which gave the maximum discernible particle diameter. The horizontal line was then compared to the TEM image scale bar for pixel-to-pixel correlation to determine the particle size distribution. The average particle size is reported as the diameter with standard deviation. Size analyses were done on a minimum of three replicate samples. The JEOL-2010F was used in high-angle dark-field scanning TEM (dark-field STEM) to minimize phase-contrast issues that occurred with the JEOL-3010. X-ray energy-dispersive spectroscopy and selected area electron diffraction (SAED) were done on the JEOL-3010.

G. UV/Vis Absorbance Spectroscopy. The UV/vis absorbance of films was measured using a standard instrument (model Cary 300 series; Varian) equipped with a solid sample holder and sample masking area of 1 cm^2, as previously described (31).

III. RESULTS AND DISCUSSION

PbS clusters were prepared in the gas phase by the CBD source shown in Figure 1 and then deposited both alone and as NCs in combination with either TiOPc or 6T. Experiments first examined the charge state, charge distribution, and energy distribution of the $(PbS)_n$ cluster beam. Embedded in TiOPc or 6T, the PbS NC shape, size, and crystallinity were then observed using various techniques in TEM. Elemental and chemical analyses of the PbS NCs embedded in organic films were examined by XPS and energy-dispersive spectroscopy. Finally, the UV/vis absorbance was measured for TiOPc films with and without PbS NCs.

A. Charge State, Charge Fraction, and Energy Distribution of Gaseous $(PbS)_n$. The $(PbS)_n$ cluster beam was found to be composed of neutral species and, at most, no more than a few percent of negatively charged $(PbS)_n^-$ cluster ions and electrons. There was no measurable positive ion current. The $(PbS)_n^-$ beam current was measured via a picoammeter connected to the sample holder during film deposition, both with and without biasing of a set of grids for retarding field measurements. The $(PbS)_n^-$ beam kinetic energy distribution peaked at 30 eV and then tailed off near 130 eV (see Figure S1 in the Supporting Information). These measurements were made in the absence of organic deposition, and their details are given below. Evidence confirming the PbS composition of the cluster beam via analysis of the deposited films is provided in the next section.

The total current of $(PbS)_n^-$ cluster ions and electrons in the beam was measured to be in the range of tens of nanoamperes. The $(PbS)_n^{0,-}$ cluster beam was further characterized by deposition onto a QCM without any retarding of the potential applied to a grid placed in front of the QCM. A −300 V retarding potential was then applied to the retarding grid to eliminate the negative clusters and any electrons in the beam while continuing to monitor the CBD rate. These retarding field measurements found no difference in the deposition rate for the charged versus neutral plus charged beam, which, given the error in the measurement, indicated that the negative cluster ion fraction was less than a few percent of the total beam.

The flow rates, types, and ratios of gases introduced into a CBD source also affect cluster formation. For example,

excessive pressure in the condensation region of the source can suppress aggregation and nucleation (27, 28). The use of reactive gases such as H_2S obviously affects cluster formation. The QCM measurements of $(PbS)_n$ beam deposition (see Figure S2a in the Supporting Information) showed an ~30% decrease in the deposition rate as the H_2S/Ar ratio was increased from 0.5:1 to 2:1. The effect of the H_2S/Ar ratio on the surface chemistry is discussed further below. However, even the less dramatic change in the noble gas type to He prevented the formation of observable NCs upon deposition (data not shown).

B. Shape, Size, and Crystallinity of PbS NCs Deposited into Organic Films. Prior work found that an organic matrix was needed for clusters generated by CBD to form NCs upon deposition into a film (20), so the $(PbS)_n$ cluster beam was used to deposit PbS NCs into TiOPc or 6T. TEM images of PbS NCs deposited in a TiOPc matrix, shown in Figure 2a, indicate roughly spherical NCs evenly dispersed throughout the film. The PbS NCs are relatively densely packed in the TiOPc films, with an average particle spacing of ~4.1 ± 2.1 nm in Figure 2a. There was little NC agglomeration, allowing the NCs to retain their discrete properties within the TiOPc matrix. The NC size distribution shown in Figure 2b indicates a narrow size range with a mean diameter of ~2.9 ± 0.6 nm.

The high-resolution TEM image of an individual PbS NC is shown in the inset of Figure 2a, with the appearance of lattice fringes providing evidence for PbS crystallinity. Additional evidence for NC crystallinity is given in Figure 2c by SAED recorded by the TEM. The diffuse, broad diffraction rings resulted from the relatively small size of NCs and their surface reactions with the organic matrix, which lead to surface relaxation of the crystalline lattice (42). It appears that the small NC sizes and the thinness of these films thwarted attempts to observe NC crystallinity via X-ray diffraction (data not shown).

PbS NCs deposited into 6T by CBD led to similar NC sizes, crystallinity, and spacings (see Figure S3 in the Supporting Information). TEM found a narrow size range of 2−5 nm PbS NCs embedded into the 6T matrix. High-resolution TEM displays a crystalline and spherical PbS NC with a 3.5 ± 0.9 nm diameter typical of all of the PbS NCs observed in 6T. PbS NCs were also well dispersed throughout the 6T film, showing little agglomeration.

Attempts were made to vary the size distribution of the PbS NCs within the organic films. The average PbS diameter was hypothesized to increase by accelerating particle condensation during cluster formation. In the inner chamber, the cooling temperature range in the condensation region (see Figure 1) was lowered to ~250 K in an attempt to increase cluster condensation. Several experiments were also performed at several cooling temperatures while all other parameters were kept constant, but TEM images revealed no difference in the particle size distributions (data not shown).

As the cluster transport distance and time in the condensation region of a CBD source increase, the resultant increase in the number of cluster collisions leading to nucleation results in the formation of larger particles (27, 28). Therefore, the path length was varied from 20 to 40 cm to examine its effect on the PbS cluster size and density within the PbS/6T film (see Figure S3 in the Supporting Information). However, the histograms in Figure S3 in the Supporting Information show that the NC size distribution within the 6T film was

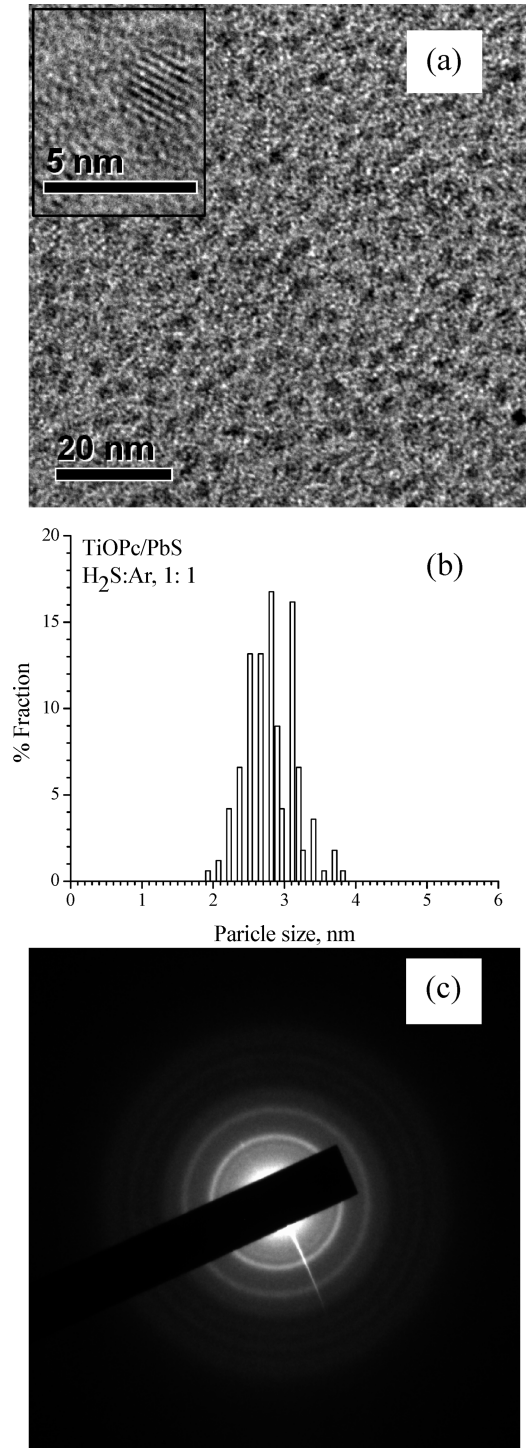

FIGURE 2. (a) TEM image of PbS NCs deposited onto a TiOPc film at a H_2S/Ar ratio of 1:1. Inset: higher magnification image of an individual NC of ~2.5 nm in size, showing PbS lattice fringes. (b) PbS NC size distribution measured from the TEM image. (c) SAED pattern of PbS NCs.

essentially constant at ~3.5 nm as the magnetron path length was varied from 20 to 40 cm.

Poor TEM phase contrast between the NCs and the matrix prevented observation of NCs smaller than ~2 nm, which may have biased the size distribution information obtained above from conventional TEM images. Dark-field STEM was used to overcome these phase-contrast effects and allowed the detection of NCs as small as 1 nm. PbS NCs appear distributed throughout the PbS/6T film in dark-field STEM images (see Figure S3, top panel, in the Supporting Information), but scale calibration difficulties prevented the determination of accurate size distributions.

Increasing the path length of the magnetron decreased the cluster deposition rate into the film (see Figure S2b in the Supporting Information): the $(PbS)_n^{0,-}$ deposition rate was 3 nm h^{-1} at 20 cm but decreased to 0.7 nm h^{-1} as the path length was increased to 70 cm. The drop in the deposition rate with the path length is consistent with observations of the NC density by TEM, which was lowest at the longest path length (see Figure S3, bottom panels, in the Supporting Information).

C. Chemical Analysis of PbS NCs Deposited in Organic Films. XPS and energy-dispersive spectroscopy were used to examine and confirm the presence of PbS NCs deposited into the organic matrices through elemental and chemical analyses of the films. The NCs were studied in the matrix because otherwise their discrete properties would be suppressed by agglomeration, which would form a film resembling bulk PbS. Pb/S stoichiometry was measured as ~1:1 (within error) via XPS at H_2S/Ar ratios of 1:1 to 2:1 in the CBD source, as shown in Figure 3a. Lowering the H_2S/Ar ratio to 0.5:1 reduced the Pb/S stoichiometry below 1:1, to 0.8 for TiOPc and 0.5 for 6T. The elemental composition of NCs fabricated with different H_2S/Ar gas ratios in both matrices, TiOPc and 6T, was determined from ratios of Pb $4f_{7/2}$ to S $2p_{3/2}$ XPS core level peak areas, shown in Figure 3b,c.

Control experiments were performed to probe changes in TiOPc-only films upon exposure to H_2S gas without magnetron sputtering of the Pb target. XPS analysis indicated no S incorporation in these films. It follows that S was only contained within the PbS NCs observed by TEM in the organic films. X-ray energy-dispersive spectra (see Figure S4 in the Supporting Information) also displayed the dominant Pb X-ray emission lines at 2.36, 10.54, 12.60, and 14.71 keV corresponding to the M_α, L_α, L_β, and L_γ transitions, respectively. The presence of these peaks indicated that the features in TEM ascribed to PbS NCs did, in fact, contain Pb. However, the presence of S X-ray emission at 2.31 and 2.46 keV for the K_α and K_β transitions, respectively, could not be discerned in the energy-dispersive spectra because of overlap with the Pb emission line at 2.36 keV.

Various changes in the XP spectra core levels appeared when PbS NCs were introduced into the TiOPc films. Figure 4 displays the C 1s and O 1s core levels of TiOPc films in the (a and c) absence and (b and d) presence of PbS NCs. C 1s core level spectra for TiOPc always show distinct

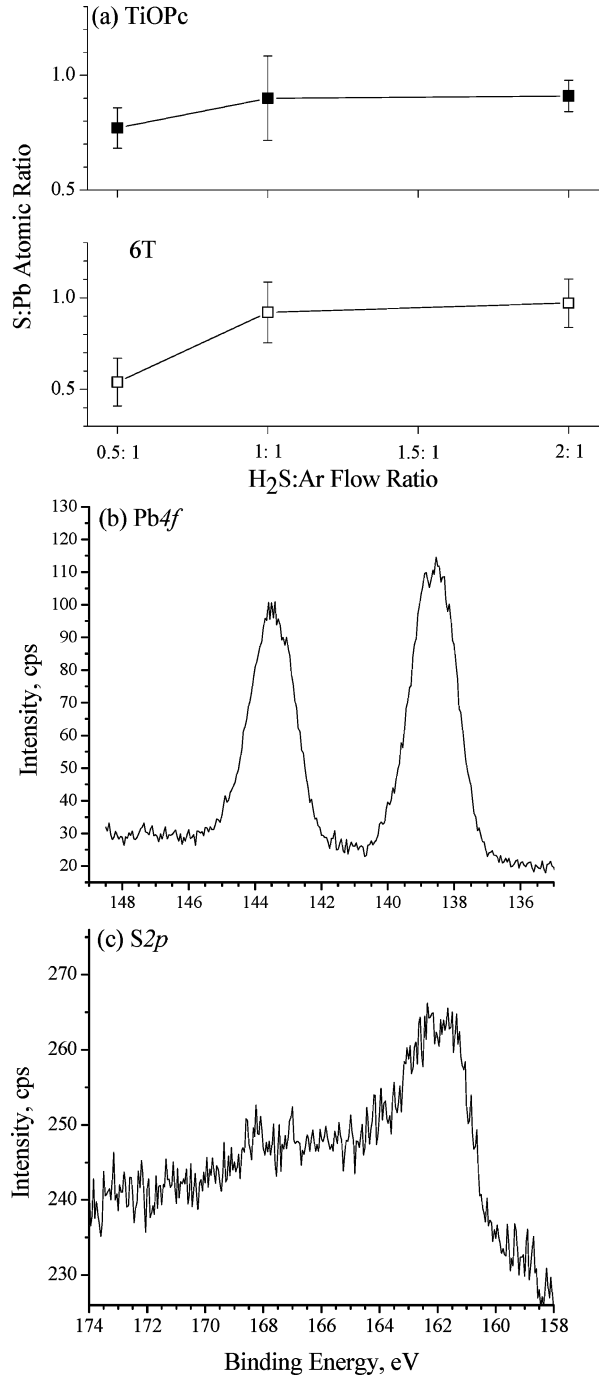

FIGURE 3. (a) Pb/S ratio as a function of the H_2S/Ar flow ratio in the CBD source measured using Al K_α XPS. (b) Pb 4f and (c) S 2p XPS core levels shown for PbS NCs deposited into TiOPc at a 1:1 H_2S/Ar gas flow ratio.

features due to contributions from the aliphatic and pyrrole C atoms in the molecule appearing at 285.0 and 286.4 eV, respectively (31). Additional spectral features due to satellites of benzene ($S_{c\text{-}2}$) and pyrrole ($S_{c\text{-}1}$) appear in the C 1s core level spectra of TiOPc at 286.9 and 288.3 eV, respectively. The C 1s core levels displayed a reduced intensity for the pyrrole feature upon introduction of PbS NCs into the TiOPc films and a general broadening of all components: both effects are attributed to the presence of S in the chemical environment. Specifically, S from PbS NCs bonded to the C

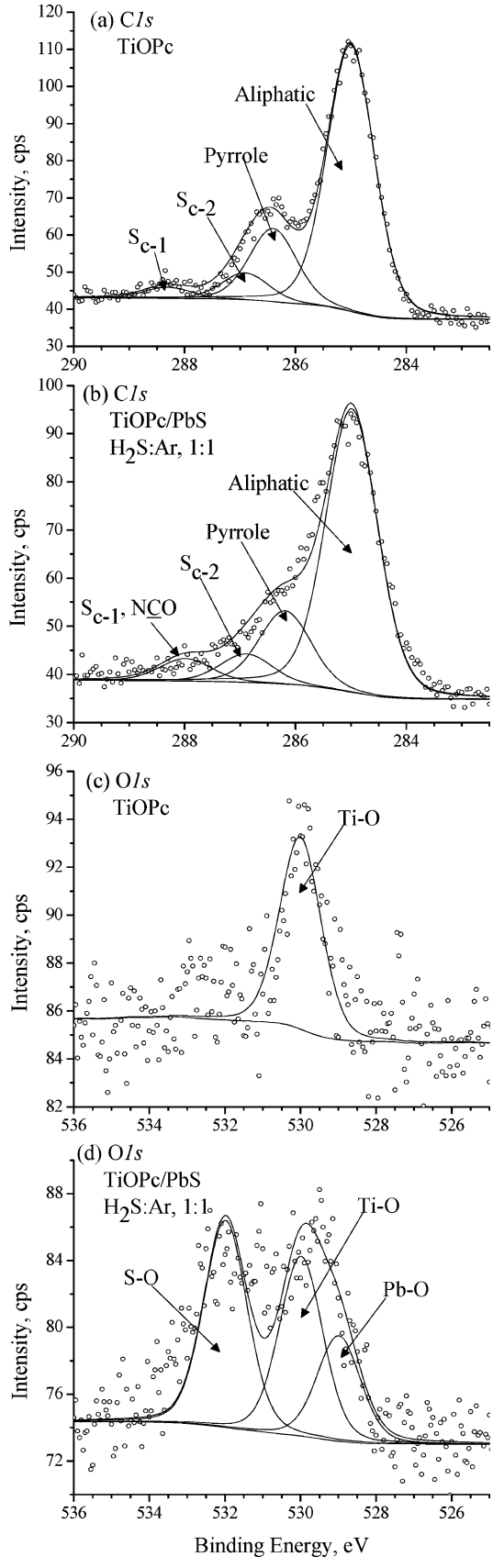

FIGURE 4. (a and b) C 1s and (c and d) O 1s XPS core levels with and without PbS NCs embedded in the TiOPc matrix (H_2S/Ar gas flow ratio of 1:1). Satellites of benzene and pyrrole are labeled S_{c-2} and S_{c-1}, respectively, while NCO corresponds to oxidized pyrrole.

atoms in the pyrrole ring of TiOPc, thereby reducing the pyrrole feature while increasing the aliphatic C feature.

An increased intensity at or near the pyrrole satellite peak upon introduction of PbS NCs is also observed in Figure 4b and is attributed to the oxidation of some pyrrole C atoms (labeled NCO). Phthalocyanines have previously shown this behavior in the presence of O when deposited on ITO-coated glass, where O attached to the TiOPc at the pyrrole ring and led to the formation of carboxyl groups (43). The behavior of the O 1s core levels further supported these arguments, indicating both oxidation and strong interaction of TiOPc with PbS NCs. A sole O 1s core level feature at 530 eV due to Ti−O from the TiOPc-only film is shown in Figure 4b. The O 1s core level upon introduction of PbS NCs displays additional components at 529 and 532 eV attributed to lead oxide (37, 44) and sulfur oxide (45), shown in Figure 4d. Oxygen binding also broadened the Pb 4f core level shown in Figure 3b, which displays the unresolved Pb $4f_{7/2}$ and Pb $4f_{5/2}$ spin orbit features at 138.5 and 143.5 eV, respectively. Some of the various oxygenated components arose from NC binding to the O in TiOPc, but others arose from atmospheric oxygen exposure during sample transfer.

The S peak near 161 eV in the S 2p XPS core level in Figure 3c was due to S bound to Pb in the core of the PbS NCs. The high-binding-energy tail on the S 2p peak indicates the presence of additional S components, but the width of this tail and overlap with the inelastically scattered photoelectrons from the Pb 4f region prevented accurate peak deconvolution. This problem was addressed by the use of lower-energy soft X-ray photons for excitation. Soft-XPS using 200 eV photons provided more surface sensitivity during analysis of the PbS/TiOPc film core levels by sampling predominantly from the top ~1 nm of the film's surface (36, 46). Defining the sampling depth as 3 times the inelastic mean-free path of Pb and S electrons moving through the TiOPc matrix allowed the sampling depth for S 2p photoelectrons to be calculated (47, 48) as 11 nm after excitation with 1486.7 eV photons from the Al K_α X-ray source used above for XPS. By contrast, the sampling depth was calculated as 0.8 nm for 200 eV photons. Similar values were calculated for Pb 4f photoelectrons.

Figure 5 displays the soft-XPS S 2p core levels from the PbS/TiOPc films prepared with different NC stoichiometries. The soft-XPS S 2p peaks display much more pronounced higher-binding-energy components when compared with the Al K_α XPS shown in Figure 3c. Additionally, soft-XPS showed that CBD clearly tuned the NC surface chemistry through variations of the reactive gas flows, as seen in Figure 5a−c. The S 2p spectra were fitted for four components shown in Figure 5: S_{core} at 161.0 eV due to sulfide (S^{2-}) bound to Pb^{2+} in the NC core (34−37); S_{surf} at 162.0 eV due to S at the NC surface (49, 50); S_{TiOPc} at 164.0 eV due to S bound to O at the NC surface (25, 43, 45, 49−51); S_{SOx} at 168.0 eV due to SO_4 and with a possible contribution on the low-binding-energy side from SO_3 (45, 50, 52). S_{SOx} resulted from air oxidation of the samples. All four peak components

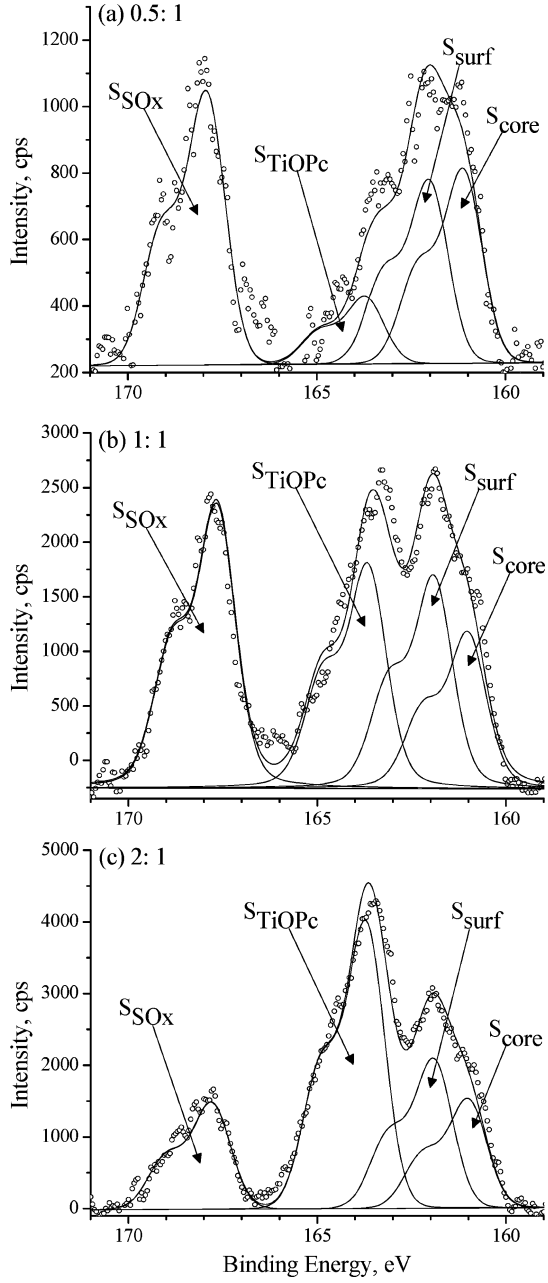

FIGURE 5. Soft-XPS recorded with 200 eV energy photons of the S 2p region of PbS NC/TiOPc films using H_2S/Ar gas flow ratios of (a) 0.5:1, (b) 1:1, and (c.) 2:1. See the text for peak assignments: S_{core} due to sulfide (S^{2-}) bound to Pb^{2+} in the NC core; S_{surf} due to S at the NC surface; S_{TiOPc} due to S bound to O at NC surface; S_{SOx} due to SO_4 with a possible contribution from SO_3.

display the characteristic 2:1 S $2p_{3/2}$/S $2p_{1/2}$ spin−orbit splitting feature.

The relative intensities of the S 2p components in Figure 5 varied with the NC stoichiometry, as controlled by variation of the H_2S/Ar gas ratio from 0.5:1 to 2:1 in the CBD source. In particular, varying the H_2S/Ar ratios during PbS NC fabrication led to a strong increase in the S_{TiOPc} component at 2:1 and, thus, influenced the NC surface chemistry. Specificially, the S_{TiOPc} component increased with the H_2S/Ar ratio, indicating that the NC surface varied from Pb-rich

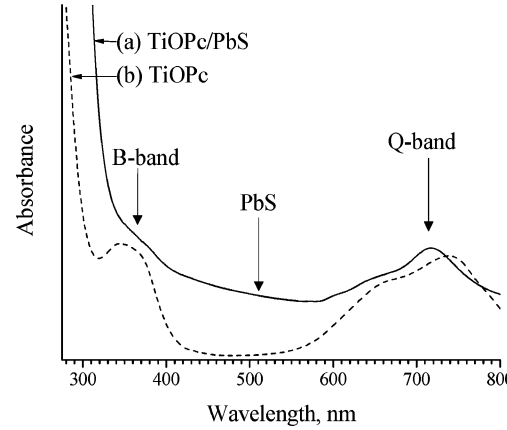

FIGURE 6. UV/vis absorbance spectra of (a) PbS NCs in a TiOPc film (solid line) and (b) a TiOPc evaporated film (dashed line) deposited on ITO-coated glass.

to S-rich. By contrast, the S_{core} and S_{surf} components remained relatively unaltered during the increase in the H_2S/Ar ratio.

XPS spectra for PbS NCs deposited in the 6T matrix were also recorded (see Figure S5 in the Supporting Information). These films were prepared under identical experimental conditions with the same H_2S/Ar gas ratio of 1:1 used above. S 2p core levels from Al K_α XPS show features for the PbS NC at 161 eV and S from 6T at 164 eV (20, 53). However, the use of S 2p core levels to probe the PbS NC interaction with the 6T matrix was masked by the S feature from the 6T matrix, so soft-XPS data are not presented for those samples. Oxidation of PbS NCs in 6T was not seen in the XPS spectra, consistent with the known ability of 6T films to resist oxidation (29).

D. UV/Vis Absorbance of PbS NCs Deposited in Organic Films. Figure 6 shows the UV/vis absorbance spectra of TiOPc in the (a) presence and (b) absence of PbS NCs. The spectra show a Q band at ~734 nm and a B band at ~340 nm, which is typical of phthalocyanines (31). The broad-band absorption from the PbS NCs appearing at wavelengths longer than ~400 nm is consistent with the absorption observed for colloidally prepared PbS NCs (20, 54). The TiOPc film with PbS NCs showed a ~20 nm blue shift in the Q-band maxima from ~734 to ~714 nm, which can arise from face-to-face stacking of adjacent TiOPc molecules (31) apparently induced by the presence of PbS NCs.

IV. CONCLUSIONS

CBD was used to deposit 3−4-nm-diameter spherical PbS NCs into organic films. This method allowed tuning of the NC surface chemistry by variation of the reactive gas conditions in the CBD source. Prior work examining NC surface chemistry utilized colloidal synthetic strategies in which ligands control the surface chemistry (7, 13−15). The use of CBD demonstrates control of the NC surface chemistry. CBD also opens up new manufacturing strategies for these important materials by ready incorporation with other vacuum-based deposition and lithography processes. A further reduction of the organic matrix deposition rate should allow for the production of closely packed films of

PbS NCs analogous to those synthesized by colloidal techniques (1, 7, 16, 17). Ongoing work is examining the photovoltaic properties of the PbS NC−organic films produced here.

Finally, the CBD method can be readily expanded to produce a wide variety of metal, semiconductor, and insulator NCs (26−28). However, the use of an organic or other matrix is needed to isolate the deposited clusters and preserve their distinct structures without problems of NC agglomeration (20).

Acknowledgment. This work was supported by the U.S. Department of Defense under Contract W81XWH-05-2-0093. This work is based, in part, upon research conducted at the Synchrotron Radiation Center, University of Wisconsin—Madison, which is supported by the National Science Foundation under Award DMR-0537588. The authors thank Mark Bissen, Dan Wallace, and Mary Severson for assistance at the Synchrotron Radiation Center with the soft-XPS experiments. Finally, the authors thank Alan Nicholls and Ke-Bin Low in the Research Resources Center of the University of Illinois at Chicago for their assistance and helpful discussions regarding TEM.

Supporting Information Available: Beam current and kinetic energy distribution for negative PbS clusters (Figure S1), effect of the H_2S/Ar gas flow ratio and magnetron path length in the CBD source on the PbS NC deposition rate (Figure S2), density and size distributions of PbS NCs as a function of the varying magnetron path length in CBD as measured by TEM as well as dark-field STEM at one path length (Figure S3), X-ray energy-dispersive spectra of PbS NCs in 6T and TiOPc (Figure S4), and Pb 4f and S 2p core level X-ray photoelectron spectra for PbS NCs deposited into 6T (Figure S5). This material is available free of charge via the Internet at http://pubs.acs.org.

REFERENCES AND NOTES

(1) Sargent, E. H. *Adv. Mater.* **2008**, *20*, 3958, and references cited therein.
(2) Wise, F. W. *Acc. Chem. Res.* **2000**, *33*, 773.
(3) Cademartiri, L.; Montanari, E.; Calestani, G.; Migliori, A.; Guagliardi, A.; Ozin, G. A. *J. Am. Chem. Soc.* **2006**, *128*, 10337.
(4) McDonald, S. A.; Konstantatos, G.; Zhang, S.; Cyr, P. W.; Klem, E. J. D.; Levina, L.; Sargent, E. H. *Nat. Mater.* **2005**, *4*, 138.
(5) Klimov, V. I. *Appl. Phys. Lett.* **2006**, *89*, 123118.
(6) Hanna, M. C.; Nozik, A. J. *J. Appl. Phys.* **2006**, *100*, 074510.
(7) Nozik, A. J. *Chem. Phys. Lett.* **2008**, *457*, 3, and references cited therein.
(8) Nair, G.; Bawendi, M. G. *Phys. Rev. B* **2007**, *76*, 081304(R).
(9) Trinh, M. T.; Houtepen, A. J.; Schins, J. M.; Hanrath, T.; Piris, J.; Knulst, W.; Goossens, A. P. L. M.; Siebbeles, L. D. A. *Nano Lett.* **2008**, *8*, 1713.
(10) Watt, A. A. R.; Blake, D.; Warner, J. H.; Thomsen, E. A.; Tavenner, E. L.; Rubinsztein-Dunlop, H.; Meredith, P. *J. Phys. D: Appl. Phys.* **2005**, *38*, 2006.
(11) Jiang, X.; Lee, S. B.; Altfeder, I. B.; Zakhidov, A. A.; Schaller, R. D.; Pietryga, J. M.; Klimov, V. I. *SPIE* **2005**, *5938*, 57.
(12) Cui, D.; Xu, J.; Zhu, T.; Paradee, G.; Ashok, S.; Gerhold, M. *Appl. Phys. Lett.* **2006**, *88*, 183111.
(13) Dissanayake, D. M. N. M.; Hatton, R. A.; Lutz, T.; Giusca, C. E.; Curry, R. J.; Silva, S. R. P. *Appl. Phys. Lett.* **2007**, *91*, 133506.
(14) Fritz, K. P.; Guenes, S.; Luther, J.; Kumar, S.; Sariciftci, N. S.; Scholes, G. D. *J. Photochem. Photobiol. A: Chem.* **2008**, *195*, 39.
(15) Kim, S. J.; Kim, W. J.; Cartwright, A. N.; Prasad, P. N. *Appl. Phys. Lett.* **2008**, *92*, 191107.
(16) Koleilat, G. I.; Levina, L.; Shukla, H.; Myrskog, S. H.; Hinds, S.; Pattantyus-Abraham, A. G.; Sargent, E. H. *ACS Nano* **2008**, *2*, 833.
(17) Luther, J. M.; Law, M.; Beard, M. C.; Song, Q.; Reese, M. O.; Ellingson, R. J.; Nozik, A. J. *Nano Lett.* **2008**, *8*, 3488.
(18) Asunskis, D. J.; Bolotin, I. L.; Hanley, L. *J. Phys. Chem. C* **2008**, *112*, 9555, and references cited therein.
(19) Steckel, J. S.; Yen, B. K. H.; Oertel, D. C.; Bawendi, M. G. *J. Am. Chem. Soc.* **2006**, *128*, 13032.
(20) Asunskis, D. J.; Bolotin, I. L.; Wroble, A. T.; Zachary, A. M.; Hanley, L. *Macromol. Symp.* **2008**, *268*, 33.
(21) Heine, J. R.; Rodriguez-Viejo, J.; Bawendi, M. G.; Jensen, K. F. *J. Cryst. Growth* **1998**, *195*, 564.
(22) Amirav, L.; Lifshitz, E. *J. Phys. Chem. C* **2008**, *112*, 13105.
(23) Cui, T.; Cui, F.; Zhang, J.; Wang, J.; Huang, J.; Lu, C.; Chen, Z.; Yang, B. *J. Am. Chem. Soc.* **2006**, *128*, 6298.
(24) Nikolaeva, E. V.; Ozerin, S. A.; Grigoriev, A. E.; Grigoriev, E. I.; Chvalun, S. N.; Gerasimov, G. N.; Trakhtenberg, L. I. *Mater. Sci. Eng.* **1999**, *C 8−9*, 217.
(25) Nanda, K. K.; Kruis, F. E.; Fissan, H.; Acet, M. *J. Appl. Phys.* **2002**, *91*, 2315.
(26) Haberland, H.; Karrais, M.; Mall, M.; Thurner, Y. *J. Vac. Sci. Technol. A* **1992**, *10*, 3266.
(27) Bansmann, J.; Baker, S. H.; Baker, S. H.; Binns, C.; Blackman, J. A.; Bucher, J. P.; Dorantes-Dávila, J.; Dupuis, V.; Favre, L.; Kechrakos, D.; Kleibert, A.; Meiwes-Broer, K. H.; Pastor, G. M.; Perez, A.; Toulemonde, O.; Trohidou, K. N.; Tuaillon, J.; Xie, Y. *Surf. Sci. Rep.* **2005**, *56*, 189.
(28) Wegner, K.; Piseri, P.; Tafreshi, H. V.; Milani, P. *J. Phys. D: Appl. Phys.* **2006**, *39*, R439.
(29) Fichou, D.; Ziegler, C. Structure and properties of oligothiophenes in the solid state: Single crystals and thin films. In *Handbook of Oligo- and Polythiophenes*; Fichou, D., Ed.; Wiley-VCH: Weinheim, Germany, 1999; p 185.
(30) Tsuzuki, T.; Shirota, Y.; Rostalski, J.; Meissner, D. *Sol. Energy Mater. Sol. Cells* **2000**, *61*, 1.
(31) Zachary, A. M.; Choi, Y.; Drabik, M.; Bolotin, I. L.; Biederman, H.; Hanley, L. *J. Vac. Sci. Technol. A* **2008**, *26*, 212, and references cited therein.
(32) Choi, Y.; Zachary, A.; Tepavcevic, S.; Wu, C.; Hanley, L. *Int. J. Mass Spectrom.* **2005**, *241*, 139.
(33) Wijesundara, M. B. J.; Ji, Y.; Ni, B.; Sinnott, S. B.; Hanley, L. *J. Appl. Phys.* **2000**, *88*, 5004.
(34) Zhu, J.; Liu, S.; Palchik, O.; Koltypin, Y.; Gadanken, A. *J. Solid State Chem.* **2000**, *153*, 342.
(35) Chen, M.; Xie, Y.; Chen, H.; Qiao, Z.; Qian, Y. *J. Colloid Interface Sci.* **2001**, *237*, 47.
(36) Lobo, A.; Moller, T.; Nagel, M.; Borchert, H.; Hickey, S. G.; Weller, H. *J. Phys. Chem. B* **2005**, *109*, 17422.
(37) Asunskis, D. J.; Hanley, L. *Surf. Sci.* **2007**, *601*, 4648.
(38) Shinn, N. D. *Phys. Rev. B* **1988**, *38*, 12248.
(39) Schalf, R.; Parkinson, B. A.; Lee, P. A.; Nebesny, K. W.; Armstrong, N. R. *Appl. Phys. Lett.* **1998**, *73*, 1026.
(40) Szade, J.; Neumann, M.; Karla, I.; Schneider, B.; Fangmeyer, F.; Matteucci, M. *Solid State Commun.* **2000**, *113*, 709.
(41) Ratner, B. D.; Castner, D. G. Electron spectroscopy for chemical analysis. In *Surface Analysis—Techniques and Applications*; Vickerman, J. C., Reed, N. M., Eds.; John Wiley & Sons: Chichester, U.K., 1993.
(42) Zhou, X.-D.; Huebner, W. *Appl. Phys. Lett.* **2001**, *79*, 3512.
(43) Gassenbauer, Y.; Klein, A. *J. Phys. Chem. B* **2006**, *110*, 4793.
(44) Reiche, R.; Thielsch, R.; Oswald, S.; Wetzig, K. *J. Electron Spectrosc. Relat. Phenom.* **1999**, *104*, 161.
(45) Nowak, P.; Laajalehto, K. *Appl. Surf. Sci.* **2000**, *157*, 101.
(46) Laajalehto, K.; Kartio, I.; Suoninen, E. *Int. J. Miner. Process.* **1997**, *51*, 163.
(47) Tougaard, S. *J. Vac. Sci. Technol. A* **1996**, *14*, 1415.
(48) Tougaard, S. *Surf. Interface Anal.* **1998**, *26*, 249.
(49) Kulkarni, S. K.; Winkler, U.; Deshmukh, N.; Borse, P. H.; Fink, R.; Umbach, E. *Appl. Surf. Sci.* **2001**, *169−170*, 438.
(50) Clifford, J. P.; Konstantatos, G.; Johnston, K. W.; Hoogland, S.; Levina, L.; Sargent, E. H. *Nat. Nanotech.* **2008**, *4*, 40.
(51) Sun, C. Q.; Tay, B. K.; Fu, Y. Q.; Li, S.; Chen, T. P.; Bai, H. L.; Jiang, E. Y. *J. Phys. Chem. B* **2003**, *107*, 411.
(52) Becker, U.; Hochella, M. F. *Geochim. Cosmochim. Acta* **1996**, *60*, 2413.
(53) Tepavcevic, S.; Choi, Y.; Hanley, L. *Langmuir* **2004**, *20*, 8754.
(54) Hines, M. A.; Scholes, G. D. *Adv. Mater.* **2003**, *15*, 1844.

AM900301X